High-pressure behavior of disodered kesterite-type Cu$_2$ZnSnS$_4$

Ilias Efthimiopoulos[1,2] · Tim Küllmey[3] · Sergio Speziale[1] · Anna S. Pakhomova[4] · Marcel Quennet[3,5] · Beate Paulus[3] · Anna Ritscher[5,6] · Martin Lerch[6]

Abstract

We have investigated the high-pressure structural and vibrational behavior of the disordered kesterite-type Cu$_2$ZnSnS$_4$ compound at ambient temperature. Our experimental and theoretical investigations have revealed a clear structural transition to a GeSb-type phase close to 15 GPa, a tetragonally distorted variant of the NaCl-type phase. The latter transformation is accompanied by a cationic coordination increase from fourfold to sixfold with respect to the sulfur anions. In addition, a change in the compressibility rate was detected at about 8 GPa within the pressure stability range of the disordered kesterite-type phase. Upon decompression, a disordered zinc blende/sphalerite structure is recovered. We discuss our findings in close conjunction with our recent high-pressure work on the ordered Cu$_2$ZnSnS$_4$ modification.

Keywords Kesterite · Pressure · Structure · XRD · Raman

1 Introduction

The quaternary semiconductor Cu$_2$ZnSnS$_4$ has attracted considerable attention in recent years due to its potential use as a solar absorber [1, 2]. The suitability of this material in photovoltaic applications originates from its almost optimal optical band gap ($E_g \sim 1.5$ eV), its high absorption coefficient in the visible range ($\sim 10^4$ cm^{-1}), and its earth-abundant, low-cost, and non-toxic elemental constituents [3–5]. The current power conversion efficiency for the pristine Cu$_2$ZnSnS$_4$ thin films, however, has not reached the theoretical limit of $\sim 30\%$ [6]. Hence, it is essential to

explore and understand the physical properties and the phase diagram of this material further, so as to develop strategies to enhance in turn its photovoltaic performance.

From a structural aspect, Cu$_2$ZnSnS$_4$ adopts the ordered kesterite-type (KS) structure at ambient conditions (SG $I\bar{4}$, $Z=2$, Fig. 1) [7, 8]. This phase is derived from the well-known zinc blende (ZB)/sphalerite-type structure (SG $F\bar{4}2m$, $Z=4$) by doubling the respective c-unit-cell parameter, resulting from the alternating cationic arrangement of Cu/Sn and Cu/Zn layers separated by sulfur anions [9]. Consequently, all of the cations are tetrahedrally coordinated with respect to the anions. Even though the KS phase represents an ordered cationic arrangement, with each cation occupying a unique Wyckoff site, cationic disorder is quite common in this material [7, 10–13]. The most common type of disorder is associated with the mutual anti-site exchange of the Cu$^+$ and Zn^{2+} cations within the $z = 1/4$ and $z = 3/4$ layers, which results in a disordered kesterite-type structural configuration (DKS) with slightly higher symmetry compared to KS (SG $I\bar{4}2m$, $Z=2$, Fig. 1). This type of disorder leads also to a reduction of the band gap E_g by up to ~ 0.2 eV [14, 15].

Some interesting observations were made regarding the compressibility behavior and structural transitions of the KS and DKS phases under pressure. In particular, application of compressive stress was predicted to increase the E_g of Cu$_2$ZnSnS$_4$, whereas a KS → stannite structural transition was found at about 32 GPa from theoretical studies [16–18].

✉ Ilias Efthimiopoulos
iliefthi@gfz-potsdam.de

1. GFZ German Research Center for Geosciences, Telegrafenberg, 14473 Potsdam, Germany

2. Institut Für Physik, Universität Greifswald, Felix-Hausdorff-Str. 6, 17489 Greifswald, Germany

3. Institut Für Chemie Und Biochemie, Freie Universität Berlin, Takustr. 3, 14195 Berlin, Germany

4. Deutsches Elektronen-Synchrotron, PETRA III, 22607 Hamburg, Germany

5. Helmholtz-Zentrum Berlin Für Materialien Und Energie, Hahn-Meitner-Platz 1, 14109 Berlin, Germany

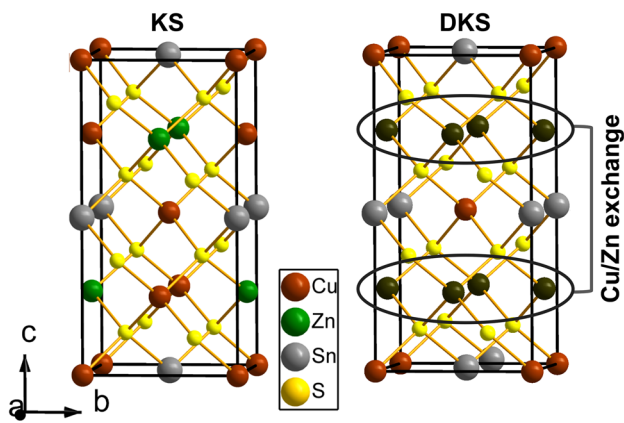6. Institut Für Chemie, Technische Universität Berlin, Straße des 17. Juni 135, 10623 Berlin, Germany

Fig. 1 Unit cell of the kesterite (KS, SG $I\bar{4}$, $Z = 2$, left) and disordered kesterite (DKS, SG $I\bar{4}2m$, $Z = 2$, right) Cu_2ZnSnS_4 modifications. The brown, green, gray, yellow, and black spheres represent Cu^+, Zn^{2+}, Sn^{4+}, S^{2-}, and mixed Cu^+/Zn^{2+} ions, respectively. Notice that in the KS structure, the Cu^+ and Zn^{2+} cations lying in the same plane occupy the distinct Wyckoff sites 2c and 2d, respectively. In the DKS structure on the other hand, the respective Cu^+ and Zn^{2+} cations are randomly distributed in these two positions, leading to a change in the space group from $I\bar{4}$ to $I\bar{4}2m$, whereas the Wyckoff positions 2c and 2d transform to position 4d

Our recent combined experimental and ab initio computational investigations on the KS Cu_2ZnSnS_4, however, dismissed the aforementioned KS → stannite transition; on the contrary, a concomitant structural and electronic transformation toward a metallic GeSb-type phase (SG $I4/mmm$, $Z = 2$), a distorted variant of the NaCl-type structure, was discovered close to 15 GPa [19, 20]. A closer inspection of the KS compressibility behavior, however, revealed clear discontinuities in the compressibility of the tetragonal KS a- and c-axis close to 6–8 GPa, whereas no visible effect was detected in the KS volume [20]. Such behavior is known to reflect (subtle) structural-related transitions in materials [21–23]. Even though the reason for this effect in KS Cu_2ZnSnS_4 is not fully understood, a plausible scenario put forward earlier involved a pressure-activated Cu/Zn cationic disorder [19, 20].

Partly motivated by our aforementioned high-pressure studies on the KS modification, and given that in the majority of synthetic Cu_2ZnSnS_4 samples the Cu/Zn disorder is always present to some extent [24–26], we have investigated the pressure-induced structural and vibrational behavior of the DKS Cu_2ZnSnS_4 compound by means of X-ray diffraction (XRD), Raman spectroscopy, and density functional theory (DFT) calculations. Similar to KS, DKS Cu_2ZnSnS_4 undergoes a pressure-induced DKS → GeSb-type structural transition close to 15 GPa, with a disordered ZB-type structure being recovered upon full decompression [20]. The most striking result, however, came from the close inspection of the DKS compressibility behavior; the latter revealed certain

similarities with its KS counterpart, with a clear compressibility change taking place close to 8 GPa. This compressibility change is reflected mainly in the pressure-induced behavior of the a/c axial ratio (i.e., the a- and c-axis exhibit similar compressibilities) above 8 GPa, stemming most likely from the expansion of the Sn–S bond length beyond that pressure. The latter effects are common in both the KS and DKS Cu_2ZnSnS_4 configurations. On the contrary, the clear discontinuities observed previously in the F-f plots of the KS Cu_2ZnSnS_4 modification were not detected in the DKS case, implying that a potential pressure-induced Cu/Zn disorder might be indeed at play for KS Cu_2ZnSnS_4 [20].

2 Experimental and computational details

The investigated disordered Cu_2ZnSnS_4 sample was available in polycrystalline powder form. Synthesis and characterization details can be found elsewhere [27–29].

Pressure was generated with symmetric diamond anvil cells (DACs) equipped with diamonds of 400 μm culet diameters. Drilled pre-indented rhenium gaskets with hole diameters of 150–200 μm served as sample chambers in separate runs. The ruby luminescence method was used for measuring pressure [30]. The error in pressure determination was $\Delta P \approx 0.1$ GPa for the low pressure range ($0 \leq P \leq 15$ GPa) and $\Delta P \approx 0.3$ GPa for the high pressure range ($15 \leq P \leq 27$ GPa). Argon served as a pressure transmitting medium (PTM) in all experiments, in order to facilitate direct comparison with our earlier high-pressure investigations on the ordered Cu_2ZnSnS_4 modification [19, 20].

The high-pressure Raman measurements were conducted with a Horiba Jobin Yvon LabRam HR800 VIS single-stage Raman spectrometer, equipped with a blue ($\lambda = 473$ nm) diode-pumped solid-state laser, a 20 × objective lens, an 1800 l/mm diffraction grating, and a Peltier-cooled charge-coupled device (CCD) detector. The measured frequency range was 100–800 cm^{-1}, with the collection time set to 3 accumulations of 10 min each. The incident laser power was kept below 1 mW, in order to avoid any potential damage on the sample [31]. The Raman-relevant parameters were obtained from the fitting of the Raman spectra with Lorentzian functions, accompanied by linear background correction/subtraction.

Angle-resolved high-pressure powder XRD measurements were performed at the Extreme Conditions Beamline P02.2 of PETRA III (Hamburg, Germany) [32] with an incident X-ray wavelength $\lambda = 0.289$ Å and a beam size of 2 μm × 2 μm. Two-dimensional XRD patterns were collected with a fast flat panel detector XRD1621 from PerkinElmer (2048 pixels × 2048 pixels, 200 × 200 μm^2 pixel size) and processed with the FIT2D software [33]. Refinements were performed using the GSAS + EXPGUI

software packages [34]. The Birch–Murnaghan equation of state (B–M EoS) function [35, 36] was fitted to the obtained pressure–volume (P–V) data of each Cu_2ZnSnS_4 phase. Given that the Ar PTM becomes solid at 1.4 GPa [37], we used its EoS as an additional pressure calibrant [38, 39].

The periodic density functional theory (DFT) calculations were performed with the Vienna Ab initio Simulation Package (VASP) 5.3.5 in the athermal limit [40–43]. A plane wave basis set with an energy cutoff of 550 eV with the projector-augmented wave (PAW) potentials [44, 45] was used, whereby the 4 s and 3d electrons of Cu and Zn, the 5 s, 5p, and 4d electrons of Sn, and the 3 s and 3p electrons of S were explicitly considered. The electronic convergence criteria were set at least to 10^{-5} eV, whereby the block Davidson algorithm was applied as implemented in VASP. The structural relaxation of internal and external lattice parameters was set to a force convergence of 4×10^{-2} eV/Å², performed with the conjugate gradient algorithm implemented in VASP. The freedom of spin polarization was enabled, and a Gaussian smearing approach with a smearing factor σ of 0.01 eV was utilized for all structural optimizations.

The DKS and the high-pressure GeSb-type phases of Cu_2ZnSnS_4 were treated in the same manner as stated before [15, 20, 46]. In a nutshell, for the DKS structure, we use the most stable $Cu \leftrightarrow Zn$ disorder pattern which can be found in the KS unit cell, with SG $P\bar{4}2c$ [47]. A total of 16 atoms were simulated, which corresponds to the number of atoms in the DKS unit cell ($Z=2$). On the other hand, for the GeSb-type phase, we omit the disorder in our model and calculate only one distribution of the cations (Fig. 2), rather than averaging over all possible distributions. This approach is sufficient to predict the transition pressure, since the energy differences between the different GeSb-type cationic patterns are smaller compared to the difference associated with the DKS → GeSb-type structural change. For the GeSb-type phase, we created $1 \times 1 \times 2$ supercells to match the number of atoms of the DKS phase. The cells were fully optimized with a $8 \times 8 \times 4$ k-grid constructed via the Monkhorst–Pack scheme [48] and centered at the Γ-point with the Perdew, Burke, and Ernzerhof (PBE) functional [49].

The EoS for each phase was determined by selecting volume points in a range of about ±100 Å³ around the minima. This corresponds to a pressure range of 0–100 GPa. We used a step size of 8 Å³, which led to 23 (DKS) and 24 (GeSb-type) volume points. At each volume point, we optimized the cell shape and the atomic positions. We fitted the B–M EoS function [35, 36] to the total energy E as a function of volume V for each Cu_2ZnSnS_4 phase. Then, the pressure of each volume was obtained from the $P(V)$ formulation of the same B–M EoS. Consequently, the enthalpy ($H = E + PV$) can be obtained for each phase as a function of pressure.
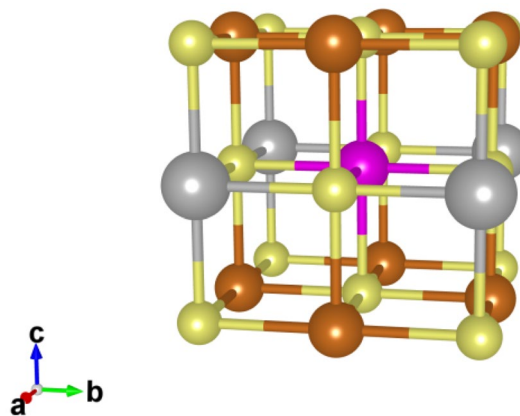

Fig. 2 The GeSb-type unit cell (SG $P4/mmm$, Z=) used in our DFT calculations. In order to match the number of atoms of the DKS unit cell, we use 2 GeSb-type unit cells stacked along the use c-axis. The brown, magenta, gray, and yellow spheres represent Cu^+, Zn^{2+}, Sn^{4+}, and S^{2-} ions, respectively. Notice that in the GeSb-type structure, all of the Cu^+, Zn^{2+}, Sn^{4+} cations are randomly distributed in the same Wyckoff site 2a, whereas the S^{2-} anions occupy the Wyckoff position 2b

3 Results and discussion

3.1 Effects of disorder in the Raman spectra of Cu₂ZnSnS₄

Before proceeding to our high-pressure results for the DKS phase, we find it useful first to briefly address the effects of the Cu/Zn anti-site disorder in the structural and vibrational properties of Cu_2ZnSnS_4. As we mentioned earlier, this type of disorder is mainly restricted in the $z=¼$ and $z=¾$ cationic planes of the $I\bar{4}$ KS phase due to the Zn_{Cu} and Cu_{Zn} anti-site exchange (Fig. 1) [11, 25, 28]. Consequently, this random distribution of the Zn^{2+} and Cu^+ cations leads to the adoption of the 'more symmetric' $I\bar{4}2m$ DKS phase. Except from the change in space group, the Cu/Zn disorder results also in an expansion of the c-axis due to the inequivalence of the Zn–S and Cu–S bond length values; the a-axis, on the other hand, does not appear to be affected [15, 46].

Regarding now the Raman activity, a total set of 14 Raman-active modes is expected for the DKS phase [24, 50]:

$$\Gamma = 2A_1 + 2B_1 + 4B_2 + 6E \tag{1}$$

whereas 15 Raman-active modes are predicted for the ordered Cu_2ZnSnS_4 KS phase [51]:

$$\Gamma = 3A + 6B + 6E \tag{2}$$

In Fig. 3, we compare the Raman spectra of the DKS and KS Cu_2ZnSnS_4 modifications measured at ambient conditions with the same experimental parameters ($\lambda = 473$ nm). Both of these KS and DKS samples were readily available
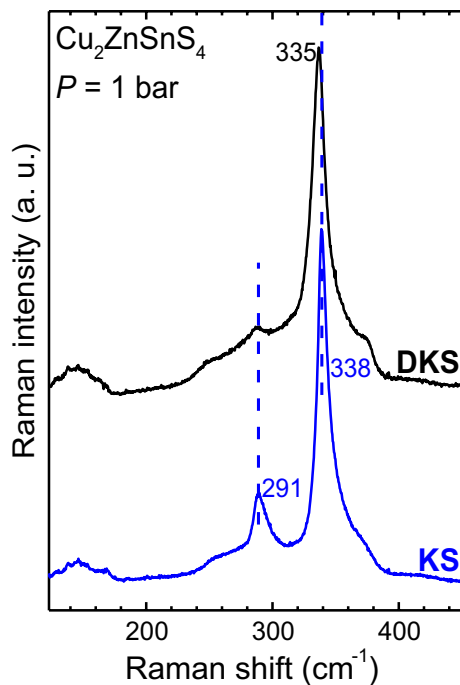
Fig. 3 Raman spectra of the DKS (black, top) and the KS (bottom, blue) Cu_2ZnSnS_4 modifications at ambient conditions ($\lambda = 473$ nm)

in polycrystalline powder form and originate from the same source [27, 28]. Generally, the ambient-pressure KS Cu_2ZnSnS_4 Raman response is consistent with the reported Raman spectra collected either with green or blue laser light excitation, with the most intense Raman features lying at ~291 cm^{-1} and ~338 cm^{-1} [13, 51–53]. These Raman peaks correspond to vibrations of A symmetry and reflect sulfur motions mainly along the *ab* plane (291 cm^{-1}) and the *c*-axis (338 cm^{-1}), respectively [54].

Coming now to the DKS sample, the main Raman-related differences between the KS and DKS modifications are: (1) the slight broadening (by ~4 cm^{-1}) and frequency downshift of the strongest 338 cm^{-1} KS peak (down to 335 cm^{-1}) and (2) the notable Raman intensity reduction of the 291 cm^{-1} KS mode. Both of these observations are consistent with the KS→DKS Raman-related changes reported in the literature [13, 31]. We should point out that the frequency drop of the strong 338 cm^{-1} KS peak (S motions along *c*-axis) upon passing to the DKS modification is connected with the expansion of the *c*-axis in the latter due to the Cu/Zn exchange. Given that the Cu/Zn cationic disorder does not seemingly affect the *a*-axis as mentioned earlier; however, no apparent frequency shift would be expected for the 291 cm^{-1} KS peak present also in the DKS phase (S motions mainly along the *ab*-plane). Contrastingly, the Cu/Zn disorder has a pronounced influence on the 291 cm^{-1} Raman peak intensity, leading to a substantial reduction (Fig. 3); the latter effect has been frequently used in the literature as a means

of monitoring the Cu/Zn disorder in Cu_2ZnSnS_4 thin films via resonant Raman scattering [55–57].

We finally mention that the presence of Cu/Zn disorder diminishes the electronic/optical band gap of Cu_2ZnSnS_4 by up to 200 meV, thus effectively affecting the photovoltaic properties of the material [5, 16, 56].

3.2 High-pressure Raman investigation of DKS Cu_2ZnSnS_4

In Fig. 4, we present collectively our high-pressure Raman spectroscopic results on DKS Cu_2ZnSnS_4. At ambient conditions, we could resolve 10 Raman-active modes for the DKS modification (Table 1) out of the 14 expected (Eq. 1). We note that only 3–4 Raman-active modes are clearly visualized in our Raman spectra (Fig. 4a); the remaining Raman features arise from the careful inspection and deconvolution of the low-intensity part of the measured spectra.

As already shown (Fig. 3), the strongest Raman features of the DKS phase at ambient conditions are the two Raman peaks at 291 cm^{-1} and 335 cm^{-1}. Both of these modes, as well as the rest of the resolved DKS Raman peaks, exhibit a rather regular behavior under compression, with their frequencies shifting to higher values upon increasing pressure (Fig. 4b). Contrary to its KS counterpart, no additional changes are observed in the DKS Cu_2ZnSnS_4 Raman spectra upon increasing pressure, e.g., the gradual emergence of a sideband in the strongest 335 cm^{-1} Raman mode as in the KS case [19].

A clear change of the DKS Cu_2ZnSnS_4 Raman spectra can be evidenced close to 15 GPa, with the vanishing of the DKS-related Raman features and the appearance of a broad band centered at ~320 cm^{-1} (Fig. 4a). In conjunction with our high-pressure XRD results presented in the next *Section*, this Raman-related change is the signature of a pressure-induced structural transition of the DKS Cu_2ZnSnS_4 compound toward a disordered GeSb-type phase, similar to KS Cu_2ZnSnS_4 [19]. We should note here that no first-order Raman activity is expected for the GeSb structure according to group theory [61]; the size inequivalence of the Cu, Zn, and Sn cations occupying the unique Wyckoff site available in the GeSb-type structure, however, may result in disorder-induced Raman activity [62].

Upon full decompression, we recover a Raman signal reminiscent of the original DKS phase, yet with substantial disorder as indicated by the broad Raman features (Fig. 4a). As we discuss below, this recovered phase corresponds to a disordered zinc blende/sphalerite-type structure, a differently disordered phase compared to the DKS Cu_2ZnSnS_4 modification. We note finally that both the GeSb-type and ZB-type Raman spectra of the DKS and KS Cu_2ZnSnS_4 modifications appear essentially identical {see Fig. 4a above & Fig. 2b from Ref. [19]}.

Fig. 4 **a** Raman spectra of Cu$_2$ZnSnS$_4$ at selected pressures ($\lambda = 473$ nm, $T = 300$ K). The black, red, and green spectra correspond to the DKS, GeSb-type, and ZB-type phases, respectively. **b** Raman mode frequency evolution as a function of pressure for the DKS (black) and the GeSb-type (red) Cu$_2$ZnSnS$_4$ phases. The solid lines passing through the data points represent polynomial least square fittings. The vertical dashed line indicates the DKS-to-GeSb-type transition
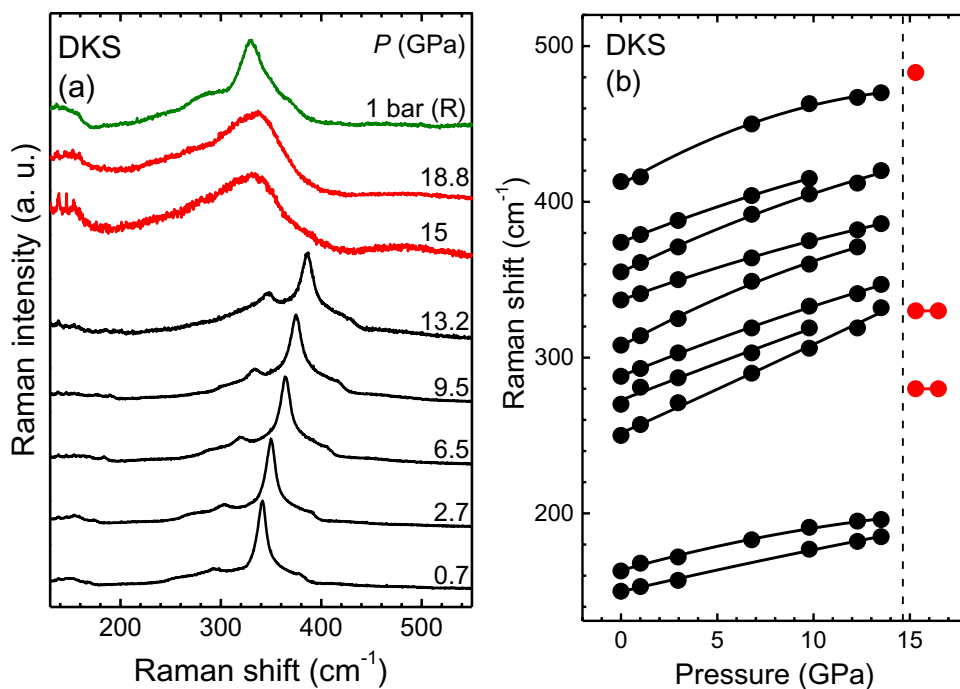

Table 1 Assignment [51, 58, 59], zero-pressure frequencies ω_0, pressure coefficients, and mode Grüneisen parameters γ_i of the Raman-active modes of DKS Cu$_2$ZnSnS$_4$ and its high-pressure GeSb-type modification.

Mode symmetry	ω_{i0} (cm^{-1})	$\partial\omega_i/\partial P$ (cm^{-1}/GPa)	$\partial^2\omega_i/\partial P^2$ (cm^{-1}/GPa^2)	γ_i
B$_2$ (E)	150 (146)	2.9 (2.7)	− 0.02	0.83
E (B)	163 (168)	3.5 (2.2)	− 0.07	0.92
E (E)	251 (254)	5.6 (5.1)	-	0.96
E (A)	273 (270)	4.8 (5.1)	-	0.76
A$_1$ (A)	290 (291)	5 (4.2)	-	0.74
B$_1$ (E)	307 (299)	6.7 (8.7)	− 0.13 (− 0.24)	0.94
A$_1$ (A)	335 (338)	4.5 (4.7)	− (− 0.09)	0.58
E (B)	355 (356)	6 (6)	− 0.09 (− 0.09)	0.73
B$_2$ (B)	374 (369)	4.9 (4.7)	-	0.56
Second-order	411 (411)^{a}	7.2 (5.8)	− 0.21 (− 0.11)	0.75
GeSb-type	280 (280)	0.1 (0.4)		
	330 (284)	0.2 (2.8)		

The Raman mode pressure dependence is given by the relation: $\omega_i(P) = \omega_{i0} + a_i P + b_i P^2$. The mode Grüneisen parameters are estimated from the equation: $\gamma_i = (B_0/\omega_{i0}) \times (\partial\omega_i/\partial P)$, where $B_0 = 43$ GPa is the bulk modulus at ambient conditions for the DKS phase, as estimated here (Table 2). The data in parentheses correspond to earlier results for the KS phase [19]

^{a}We have additionally detected a low-intensity Raman feature at 411 cm^{-1}; since no Raman activity is expected in this frequency region for either the KS or DKS-Cu$_2$ZnSnS$_4$ phases [51, 59, 60], and the 411 cm^{-1} band does not correspond to any known Cu$_2$ZnSnS$_4$-related impurity [53], we tentatively assign it as a second-order Raman feature

## 3.3 Structure of DKS Cu$_2$ZnSnS$_4$ under pressure

Following our Raman results, we have performed in situ high-pressure XRD investigations on DKS Cu$_2$ZnSnS$_4$ in order to identify the structural changes under compression. We should mention that minor traces of Cu$_2$S were detected at ambient conditions, a well-known secondary phase formed during the synthesis of Cu$_2$ZnSnS$_4$ [12].

The results are presented in Fig. 5. We can observe that the DKS phase persists up to ~ 15 GPa; at this pressure, the vanishing and merging of individual DKS Bragg peaks, as well as the appearance of novel Bragg features in the XRD patterns, denote a clear structural transition. The structural

Fig. 5 **a** Selected XRD patterns of Cu_2ZnSnS_4 at various pressures ($T = 300$ K, $\lambda = 0.289$ Å). The various phases are indicated by black (DKS), red (GeSb-type), and orange (phase mixture) lines. The red arrow indicates the most characteristic Bragg peak of the GeSb-type high-pressure phase. **b** Refined XRD patterns for the DKS (3.3 GPa, Rietveld, bottom), the GeSb-type (23.3 GPa, Le Bail, middle), and the recovered ZB-type (Le Bail, top) phases of Cu_2ZnSnS_4. Dots correspond to the measured spectra, and the red solid lines represent the best refinements. The difference spectra between the measured and the refined patterns are depicted too (blue curves). Vertical ticks mark the Bragg peak positions. Asterisks mark the strongest XRD peaks of the Cu_2S impurity
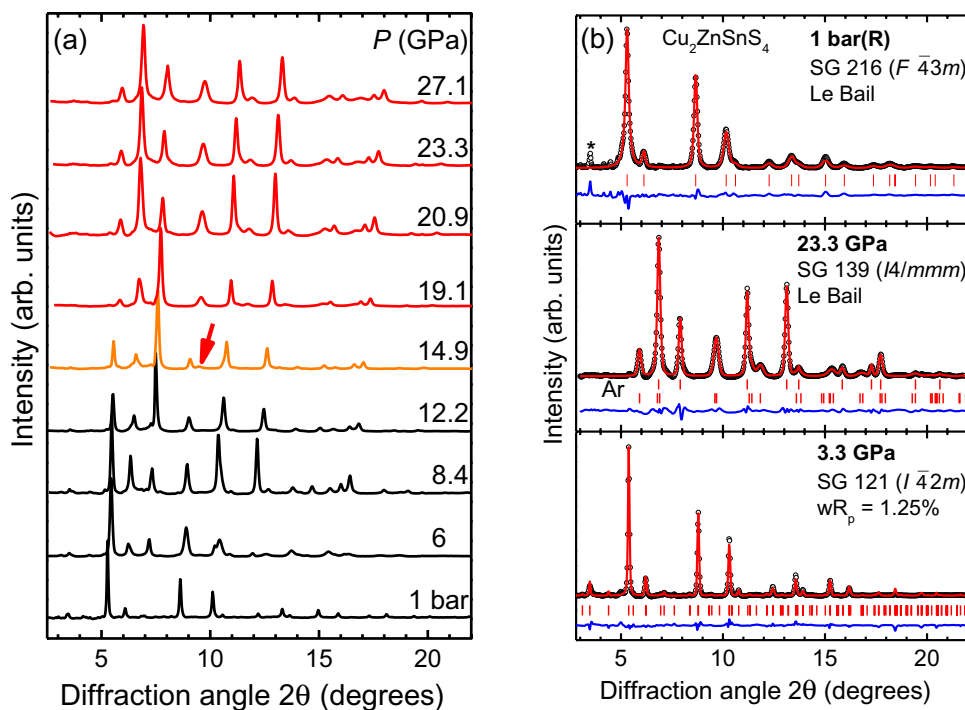
transformation is apparently completed at 19 GPa, in excellent agreement with our aforementioned Raman results, as well as the equivalent XRD investigations on the KS Cu_2ZnSnS_4 [19, 20]. As in the KS counterpart, the high-pressure phase of DKS Cu_2ZnSnS_4 is indexed to a GeSb-type structure (SG $I4/mmm$, $Z = 2$), a tetragonally distorted modification of the well-known rocksalt-type phase [63]. In this GeSb-type phase, the single cationic site is randomly occupied by the Cu^+, Zn^{2+}, and Sn^{4+} metal cations, whereas the cationic coordination increases from fourfold to sixfold with respect to the sulfur anions [20]. Finally, upon full decompression, the original DKS phase is not recovered; on the contrary, a different ZB-type structure is adopted (SG $F\bar{4}3m$, $Z = 4$), where again the Cu^+, Zn^{2+}, and Sn^{4+} cations are randomly distributed in the unique cationic site, whereas the cationic coordination is 'restored' back to fourfold with respect to the anions. The back-transformation to a disordered ZB-type phase was also detected in the case of the KS Cu_2ZnSnS_4 [20] and is consistent with our Raman observations (Fig. 4a).

In Fig. 6, we plot the extracted structural parameters for the DKS and GeSb-type phases of Cu_2ZnSnS_4. As we can observe, the DKS→GeSb-type structural transition is accompanied by a ~14% volume change at the transition point. The latter volume drop results from steric effects, due to the increase in the cationic coordination with respect to the S^{2-} anions from four to six [19, 20, 64, 65]. The B-M EoS fitting results of the P–V data for both Cu_2ZnSnS_4 phases, alongside relevant literature data, are listed in Table 2. A noteworthy observation is the large value of the

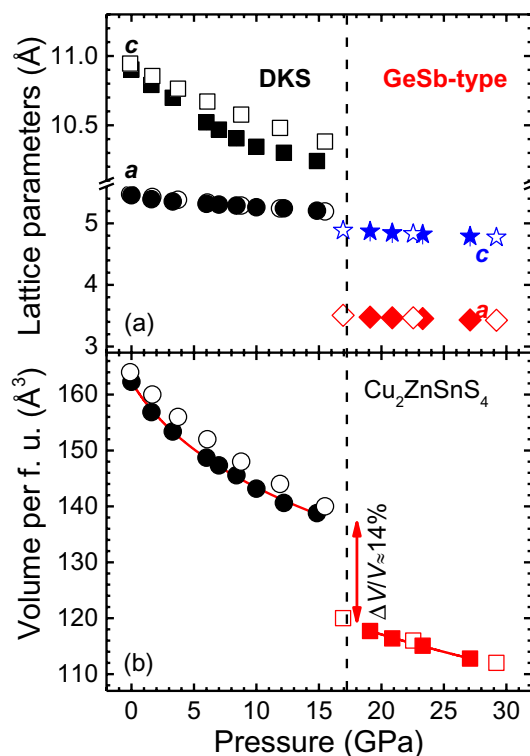**Fig. 6** **a** Lattice constants and **b** unit cell volume per formula unit as a function of pressure for the various phases of DKS-Cu_2ZnSnS_4. Closed and open symbols correspond to experimental and DFT-calculated data. Error bars lie within the symbols. The vertical dashed line marks the onset pressure of the DKS-to-GeSb-type structural transition. The solid lines represent fitted Birch-Murnaghan EoS functions

Table 2 Elastic parameters for all phases of Cu_2ZnSnS_4, resulting from the experimental P–V data fitting.

Phase	PTM	P_{Ref} (GPa)	V_{Tr}/Z (Å³)	B_{Tr} (GPa)	B'_{Tr}
DKS (exp)	Ar	10^{-4}	162.30(1)	43(5)	11(2)
DKS (DFT-PBE)	n/a	10^{-4}	163.74	68.67	4.64
KS (exp) [20]	Ar	10^{-4}	160.11(3)	74(2)	4.4(4)
KS (DFT-PBE) [18]	n/a	10^{-4}	160	56.31	N/A
KS (DFT-PBE) [20]	n/a	10^{-4}	163.75	68.64	4.64
KS (DFT-LDA) [72]	n/a	10^{-4}	150.7	89.4	N/A
SnS₂ [69]	M/E	10^{-4}	67.82(2)	28.1(6)	9.5(4)
GeSb-type (DKS)	Ar	19.1	117.72(2)	172(3)	4(fixed)
GeSb-type (KS) [20]	Ar	15.8	119.40(2)	213(4)	4(fixed)
GeSb-type (DFT-PBE)	n/a	16	120.75	298.53	2.03

Each parameter is evaluated at a reference pressure P_{Ref}

The abbreviations below stand for: n/a = not applicable, PTM = pressure transmitting medium, M/E = methanol–ethanol mixture 4:1, KS = kesterite, DKS = disordered kesterite, and V_{Tr}/Z, B_{Tr}, and B'_{Tr} = volume per formula unit Z, bulk modulus, and its pressure derivative, respectively

DKS bulk modulus derivative $B'_0 = 11(2)$. Attempts to fit the DKS P–V data fixing the value of B'_0 between 4 and 8, a common range for various classes of materials [66], resulted in poor fits. Such large B'_0 value stems from the anisotropic compressibility of the DKS phase, which most likely leads to an increased repulsion between neighboring ions (for more details, see, e.g., Refs. [67, 68]). Such high B'_0 values appear to be the norm mostly for (quasi-)layered [23, 69] and molecular/organic materials [70, 71]. We should note here that a more 'normal' B'_0 value was previously estimated for the KS Cu_2ZnSnS_4 phase (Table 2) [21]. As we shall see in the next *Section*, this B'_0 value discrepancy follows most likely from the different compressibility behavior of the KS and DKS systems, as revealed from the respective axial compressibility plots.

In order to acquire certain insights on the aforementioned pressure-induced DKS → GeSb-type structural transition in Cu_2ZnSnS_4, we have calculated the respective enthalpies [$H(P) = E + PV$] for the starting DKS and the high-pressure GeSb-type modifications by means of DFT, where E is the internal energy (Fig. 7). As we can observe from the relative enthalpy difference ΔH between the DKS and the GeSb-type phases, the transition is predicted to take place at 16 GPa, in excellent agreement with the experimental transition pressure value (Fig. 6). The respective lattice parameters and volumes for the DKS and GeSb-type Cu_2ZnSnS_4 structures are plotted alongside their experimental counterparts in Fig. 6. Overall, we can observe a very good agreement between the experimental and calculated values, with the exception of the DKS c-axis and volume, which are overestimated within the DFT-PBE approximation [73, 74]. The respective DFT-PBE calculated volumes, bulk moduli, and bulk moduli derivatives for the DKS and GeSb-type Cu_2ZnSnS_4 phases
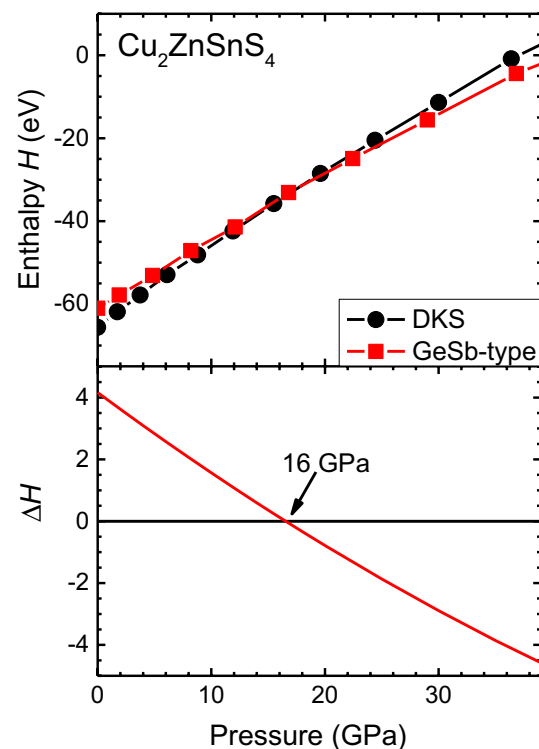

Fig. 7 Calculated enthalpies of the DKS and GeSb-type Cu_2ZnSnS_4 phases ($Z = 2$) as a function of pressure, as well as the respective enthalpy difference $\Delta H = H(\text{GeSb-type}) - H(\text{DKS})$ with respect to pressure. A phase is stable if it has a lower value of H

are listed in Table 2. We note that our calculations could not reproduce the relatively high experimental B'_0 value of the DKS Cu_2ZnSnS_4 phase, with its underestimation arising most likely from the approximations within the DFT-PBE method [75, 76].

3.4 Structural comparison between KS and DKS Cu$_2$ZnSnS$_4$ under compression

As we have discussed up to now, the DKS Cu$_2$ZnSnS$_4$ phase behaves in a rather similar manner to its KS counterpart with respect to the high-pressure structural behavior, by exhibiting the same structural transition toward a GeSb-type structure close to 15 GPa, as well as the transformation to a disordered ZB-type phase upon full decompression. Given that clear breaks/discontinuities in the compressibility of the *a*- and *c*-structural parameters of KS Cu$_2$ZnSnS$_4$ were detected earlier between 6 and 8 GPa from the normalized stress *F* as a function of the Eulerian strain f_E plots (yet not in the volume, as the two effects appeared to 'cancel' each other out) [20], we have performed a similar analysis for the DKS Cu$_2$ZnSnS$_4$. The results are plotted collectively in Fig. 8.

Even though none of the *F-f* plots displays any discontinuities for the DKS Cu$_2$ZnSnS$_4$, we can still observe some interesting features. In particular: (a) the compressibilities of the DKS *a*- and *c*-axes exhibit an apparent nonlinear *F-f* behavior, with a rate of increase up to ~8 GPa, and a plateau (*a*-axis) and upward (decrease of the *c*-axis pressure slope) behavior above that pressure point, respectively; such behavior implies that one needs to take into account higher (than third) order elastic parameters associated with the tetragonal DKS *a*-axis for approximating its pressure-induced evolution [76], (b) the DKS volume *V* exhibits a linear *F-f* dependence, indicating that the nonlinear behavior of the F_a-f_{Ea} and F_c-f_{Ec} parameters is not affecting the F_V-f_{EV} dependence, which in turn implies that a third-order B–M EoS suffices for describing the *P–V* data for the DKS Cu$_2$ZnSnS$_4$ phase (Fig. 6), and (c) the bulk modulus B_0 and its pressure derivative B'_0 values extracted from the F_V-f_{EV} analysis are virtually identical to the equivalent EoS fitting values for the DKS Cu$_2$ZnSnS$_4$ phase (Table 2). We note that our DFT calculations have failed to capture the aforementioned effects (open symbols in Fig. 8), owing probably to the approximations within the DFT-PBE method [75, 76].

The nonlinear dependence of the DKS *a*-axis compressibility, as revealed from the respective F_a-f_{Ea} plot, prompted us to examine the evolution of several relevant structural parameters as a means of rationalizing such behavior. Firstly, we have examined the evolution of the *a/c* tetragonal axial ratio for both the KS and DKS Cu$_2$ZnSnS$_4$ modifications under compression (Fig. 9). We can observe that irrespective of the PTM used, the *a/c* ratio shows a clear slope change between 6 and 8 GPa for both the KS and DKS Cu$_2$ZnSnS$_4$ samples, with the *a*- and *c*-axes exhibiting similar compressibility beyond this pressure. Furthermore, we have inspected the pressure-induced evolution of selected DKS interatomic bond lengths (Fig. 9); even though the Cu–S and (Cu/Zn)–S bond lengths shorten continuously upon compression, the
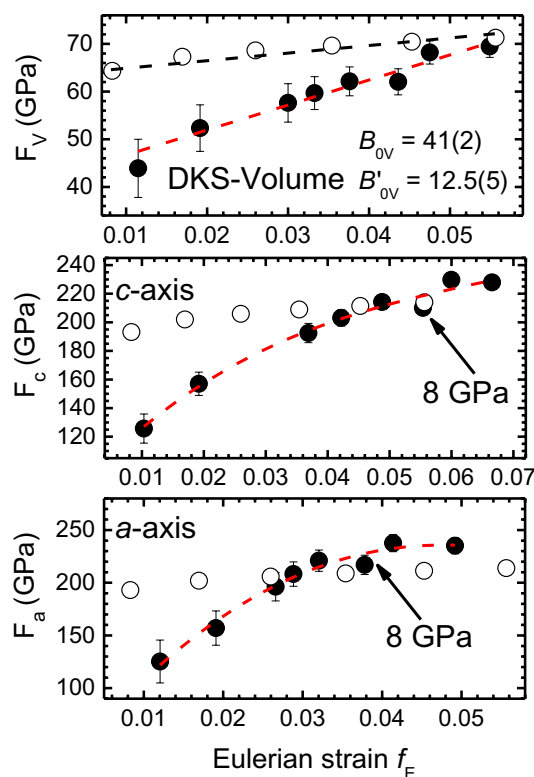
Fig. 8 Plot of the normalized stress *F* as a function of the Eulerian strain f_E for the *a*- and *c*-axes, and the volume of the DKS Cu$_2$ZnSnS$_4$ phase. The closed and open symbols correspond to experimental and calculated data, respectively. The relevant quantities are calculated from the data shown in Fig. 6 as follows [21, 77]: $f_{EV} = [(V_0/V)^{2/3} - 1]/2$ and $F_V = P/3f_{EV}(1 + 2f_{EV})^{5/2}$, where V_0 is the ambient-pressure volume of the DKS phase, *V* is the volume, and *P* is pressure; $f_{Ea} = [(a_0/a)^2 - 1]/2$, $F_a = P(ac_0/a_0c)^{2/3}/f_{Ea}(1 + 2f_{EV})^{5/2}$ for the *a*-axis (where a_0 is the ambient-pressure *a*-axis value); $f_{Ec} = [(c_0/c)^2 - 1]/2$ and $F_c = P(a_0c/ac_0)^{4/3}/f_{Ec}(1 + 2f_{EV})^{5/2}$ for the *c*-axis (where c_0 is the ambient-pressure *c*-axis value). In case of a valid third-order B-M EoS for the F_V-f_{EV} parameters (i.e., elastic energy limited to third order in strain), the latter follow a linear correlation: $F_V = B_{0V} + 1.5B_{0V}(B'_{0V} - 4)f_{EV}$

Sn–S bond length *expands* above 8 GPa, coinciding roughly with both the aforementioned *a/c*, *a*- and *c*-axes compressibility rate changes. Hence, the nonlinearity uncovered in the DKS F_a-f_{Ea} and F_c-f_{Ec} plots, as well as the change in the *a/c* axial ratio pressure dependence, appears to be connected to a pressure-induced change in the interatomic bonding (mostly involving the Sn and S ions) within the DKS Cu$_2$ZnSnS$_4$ phase.

Hence, by taking into account all of the above information, we can reach an overview of the high-pressure structural response of the DKS Cu$_2$ZnSnS$_4$ material. Its compressibility behavior can be divided in two stages: (i) For pressures below 8 GPa, the compressibility of the DKS Cu$_2$ZnSnS$_4$ phase is accommodated mainly in the *c*-axis direction, i.e., along the direction of the cation–anion–cation

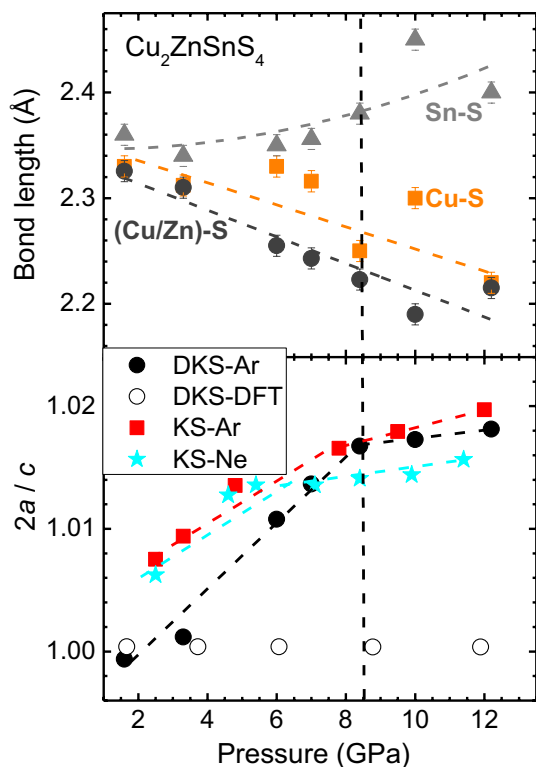**Fig. 9** Top: Selected bond lengths for the DKS Cu_2ZnSnS_4 modification against pressure increase, as extracted from the XRD measurements. Bottom: Plot of the $2a/c$ ratio for the DKS (Ar as PTM) and KS Cu_2ZnSnS_4 samples (Ar and Ne as PTM) as a function of pressure. The dashed lines are guides for the eye. The KS Cu_2ZnSnS_4 data are taken from [19, 20]. The open symbols correspond to the DFT-calculated data for the DKS Cu_2ZnSnS_4. The vertical dashed line indicates the compressibility turn point (see text for more details)

layers (Fig. 1), indicating the anisotropy of the material in terms of response to strain. (ii) For pressures above 8 GPa and below the DKS→GeSb-type structural transition occurring at ~15 GPa, the DKS Cu_2ZnSnS_4 becomes more isotropic compressibility-wise, as the rate of compression in both the *a*- and *c*-axis directions becomes almost equivalent; this similarity stems from the *expansion* of the Sn–S bond length above 8 GPa. Given that the unoccupied Sn 5p and S 3p orbitals primarily compose the conduction band of the DKS phase [20], one would expect that this Sn–S pressure-induced separation would also energetically affect the unoccupied DKS conduction band in terms of cation–anion orbital overlap. Whether this process may lead to a potential electronic topological transition (ETT) [23, 78, 79] remains to be explored.

Now that we have discussed the overall DKS Cu_2ZnSnS_4 compressibility mechanism, a direct comparison with the KS phase is in order. The two modifications exhibit a common behavior, namely the pressure dependence of the tetragonal *a/c* axial ratio (Fig. 9) and that the pressure-induced bond length evolution is similar in both KS and DKS

modifications [20], with a pressure rate change observed between 6 and 8 GPa. This implies that the potential pressure-induced electronic changes speculated above near that pressure might be *inherent* to the Cu_2ZnSnS_4 system.

On the other hand, clear discontinuities in the *F-f* plots appear only in the KS Cu_2ZnSnS_4 compound [20]. Hence, the origin behind these pressure-induced effects should be associated exclusively with the KS modification. Considering the previously reported Raman results in KS Cu_2ZnSnS_4, where a sideband of the strongest KS Raman peak mode located at 338 cm⁻¹ (Fig. 3) gradually enhanced in intensity at the expense of the 338 cm⁻¹ mode upon increasing pressure and eventually replaced it close to 6–8 GPa where the *F-f* discontinuities occur [19, 20], we tend to favor a gradual pressure-induced Cu/Zn anti-site cationic exchange (disorder) taking place in KS Cu_2ZnSnS_4 under compression. Such scenario is currently explored and will be the focus of an upcoming publication.

Finally, we mention that further compression of the DKS Cu_2ZnSnS_4 sample results in a similar behavior as its KS counterpart, i.e., the adoption of a GeSb-type structure above ~15 GPa (Figs. 5, 6), whereas a disordered sphalerite-type (ZB-type) phase is recovered upon full decompression (Fig. 5). All in all, we can conclude that the presence of Cu/Zn disorder in the starting Cu_2ZnSnS_4 compound appears to have a negligible effect in its generic high-pressure behavior; nevertheless, it needs to be pointed out that hydrostatic compression appears to favor the Cu/Zn anti-site cationic exchange (disorder) in Cu_2ZnSnS_4, a parameter which should be carefully considered for thin film applications.

4 Conclusion

In summary, we have investigated the high-pressure structural and vibrational behavior of the DKS Cu_2ZnSnS_4 compound. Our investigations revealed pressure-induced compressibility changes of the DKS *c*-axis and the *a/c* axial ratio close to 8 GPa, associated with an expansion of the Sn–S bond length. Further compression leads to a DKS→GeSb-type structural transition above 15 GPa. Upon full decompression, a disordered sphalerite-type (ZB-type) phase is recovered. Close comparison with the high-pressure behavior of the KS Cu_2ZnSnS_4 modification indicates that application of external pressure appears to favor the Cu/Zn disorder, whereas its presence appears to have a negligible effect in the overall high-pressure behavior of the structural properties of the Cu_2ZnSnS_4 system.

References

1. H. Katagiri, K. Jimbo, W.S. Maw, K. Oishi, M. Yamazaki, H. Araki, A. Takeuchi, Thin Solid Films **517**, 2455 (2009)
2. X. Liu, Y. Feng, H. Cui, F. Liu, X. Hao, G. Conibeer, D.B. Mitzi, M. Green, Progr. Photovoltaics **24**, 879 (2016)
3. J.J. Scragg, P.J. Dale, L.M. Peter, G. Zoppi, I. Forbes, Phys. Stat. Sol. (b) **245**, 1772 (2008)
4. S. Siebentritt, S. Schorr, Progr. Photovolt. **20**, 512 (2012)
5. S. Chen, X.G. Gong, A. Walsh, S.-H. Wei, Appl. Phys. Lett. **94**, 041903 (2009)
6. W. Shockley, H.J. Queisser, J. Appl. Phys. **32**, 510 (1961)
7. L. Choubrac, M. Paris, A. Lafond, C. Guillot-Deudon, X. Rocquefelte, S. Jobic, Phys. Chem. Chem. Phys. **15**, 10722 (2013)
8. S. Schorr, Sol. Energy Mater. Sol. Cells **95**, 1482 (2011)
9. S. Schorr, Thin Solid Films **515**, 5985 (2007)
10. S. Chen, X.G. Gong, A. Walsh, S.-H. Wei, Appl. Phys. Lett. **96**, 021902 (2010)
11. S. Chen, J.-H. Yang, X.G. Gong, A. Walsh, S.-H. Wei, Phys. Rev. B **81**, 245204 (2010)
12. L.E.V. Rios, K. Neldner, G. Gurieva, S. Schorr, J. Alloys Compd. **657**, 408 (2016)
13. R. Caballero, E. Garcia-Llamas, J.M. Merino, M. Leon, I. Babichuk, V. Dzhagan, V. Strelchuk, M. Valakh, Acta Mater. **65**, 412 (2014)
14. M. Grossberg, J. Krustok, J. Raudoja, T. Raadik, Appl. Phys. Lett. **101**, 102102 (2012)
15. M. Quennet, A. Ritscher, M. Lerch, B. Paulus, J. Solid State Chem. **250**, 140 (2017)
16. Y. Zhao, D. Li, Z. Liu, J. Alloys Compd. **696**, 86 (2017)
17. Y. Zhao, D. Li, Z. Liu, Mod. Phys. Lett. B **30**, 1650176 (2016)
18. C.-R. Li, Y.-F. Li, B. Yao, G. Yang, Z.-H. Ding, R. Deng, L. Liu, Phys. Lett. A **377**, 2398 (2013)
19. I. Efthimiopoulos, A. Ritscher, M. Lerch, S. Speziale, A.S. Pakhomova, H.P. Liermann, M. Koch-Müller, Appl. Phys. Lett. **110**, 041905 (2017)
20. I. Efthimiopoulos, T. Kullmey, S. Speziale, A.S. Pakhomova, M. Quennet, B. Paulus, A. Ritscher, M. Lerch, M. Koch-Müller, J. Appl. Phys. **124**, 085905 (2018)
21. C. Meade, R. Jeanloz, Geophys. Res. Lett. **17**, 1157 (1990)
22. R.J. Angel, Rev. Miner. Geochem. **41**, 35 (2000)
23. A. Polian, M. Gauthier, S.M. Souza, D.M. Triches, J.C. de Lima, T.A. Grandi, Phys. Rev. B **83**, 113106 (2011)
24. S. Schorr, G. Gurieva, M. Guc, M. Dimitrievska, A. Perez-Rodriguez, V. Izquierdo-Roca, C.S. Schnohr, J. Kim, W. Jo, J.M. Merino, J. Phys. Energy **2**, 12002 (2020)
25. S.K. Wallace, J.M. Frost, A. Walsh, J. Mater. Chem. A **7**, 312 (2019)
26. S.P. Ramkumar, A. Miglio, M.J. van Setten, D. Waroquiers, G. Hautier, G.-M. Rignanese, Phys. Rev. Mater. **2**, 085403 (2018)
27. A. Ritscher, M. Hoelzel, M. Lerch, J. Sol. St. Chem. **238**, 68 (2016)
28. A. Ritscher, J. Just, O. Dolotko, S. Schorr, M. Lerch, J. Alloys Compd. **670**, 289 (2016)
29. A. Ritscher, A. Franz, S. Schorr, M. Lerch, J. Alloys Compd. **689**, 271 (2016)
30. H.K. Mao, J. Xu, P. Bell, J. Geophys. Res. **91**, 4673 (1986)
31. M.Y. Valakh, O.F. Kolomys, S.S. Ponomaryov, V.O. Yukhymchuk, I.S. Babichuk, V. Izquierdo-Roca, E. Saucedo, A. Perez-Rodriguez, J.R. Morante, S. Schorr, I.V. Bodnar, Phys. Status Solidi RRL **7**, 258 (2013)
32. H.-P. Liermann, Z. Konopkova, W. Morgenroth, K. Glazyrin, J. Bednarcik, E.E. McBride, S. Petitgirard, J.T. Delitz, M. Wendt, Y. Bican, A. Ehnes, I. Schwark, A. Rothkirch, M. Tischer, J. Heuer, H. Schulte-Schrepping, T. Kracht, H. Franz, J. Synchrotron Rad. **22**, 908 (2015)
33. A.P. Hammersley, S.O. Svensson, M. Hanfland, A.N. Fitch, D. Hausermann, High Press. Res. **14**, 235 (1996)
34. B.H. Toby, J. Appl. Crystallogr. **34**, 210 (2001)
35. F. Birch, Phys. Rev. **71**, 809 (1947)
36. F. Birch, J. Geophys. Res. **83**, 1257 (1978)
37. S. Klotz, J.-C. Chervin, P. Munsch, G. Le Marchand, J. Phys. D Appl. Phys. **42**, 075413 (2009)
38. D. Errandonea, R. Boehler, S. Japel, M. Mezouar, L.R. Benedetti, Phys. Rev. B **73**, 092106 (2006)
39. M. Ross, H.K. Mao, P.M. Bell, J.A. Xu, J. Chem. Phys. **85**, 1028 (1986)
40. G. Kresse, J. Furthmüller, Comput. Mater. Sci. **6**, 15 (1996)
41. G. Kresse, J. Furthmüller, Phys. Rev. B **54**, 11169 (1996)
42. G. Kresse, J. Hafner, Phys. Rev. B **47**, 558 (1993)
43. G. Kresse, J. Hafner, Phys. Rev. B **49**, 14251 (1994)
44. G. Kresse, D. Joubert, Phys. Rev. B **59**, 1758 (1999)
45. P.E. Blöchl, Phys. Rev. B **50**, 17953 (1994)
46. M. Quennet, Ph. D. thesis, First Principles Calculations for the Semiconductor Material Kesterite Cu_2ZnSnS_4 and Se-Containing Derivatives, Freie Universität Berlin (2016)
47. J.J.S. Scragg, J.K. Larsen, M. Kumar, C. Persson, J. Sendler, S. Siebentritt, C. Platzer Björkman, Phys. Status Solidi. **253**, 247 (2016)
48. H.J. Monkhorst, J.D. Pack, Phys. Rev. B **13**, 5188 (1976)
49. J.P. Perdew, K. Burke, M. Ernzerhof, Phys. Rev. Lett. **77**, 3865 (1996)
50. S. Levcenko, A. Nateprov, V. Kravtsov, M. Guc, A. Perez-Rodriguez, V. Izquierdo-Roca, X. Fontane, E. Arushanov, Opt. Express **22**, A1936 (2014)
51. A. Khare, B. Himmetoglu, M. Johnson, D.J. Norris, M. Cococcioni, E.S. Aydil, J. Appl. Phys. **111**, 083707 (2012)
52. M. Dimitrievska, A. Fairbrother, X. Fontane, T. Jawhari, V. Izquierdo-Roca, E. Saucedo, A. Perez-Rodriguez, Appl. Phys. Lett. **104**, 021901 (2014)
53. P.A. Fernandes, P.M.P. Salome, A.F. da Cunha, J. Alloys Compd. **509**, 7600 (2011)
54. J.M. Skelton, A.J. Jackson, M. Dimitrievska, S.K. Wallace, A. Walsh, APL Mater. **3**, 041102 (2015)
55. K. Rudisch, A. Davydova, C. Platzer-Bjorkman, J. Scragg, J. Appl. Phys. **123**, 161558 (2018)

56. J.J.S. Scragg, L. Choubrac, A. Lafond, T. Ericson, C. Platzer-Bjorkman, Appl. Phys. Lett. **104**, 041911 (2014)
57. M. Paris, L. Choubrac, A. Lafond, C. Guillot-Deudon, S. Jobic, Inorg. Chem. **53**, 8646 (2014)
58. D. Dumcenco, Y.-S. Huang, Opt. Mater. **35**, 419 (2013)
59. M. Guc, S. Levcenko, I.V. Bodnar, V. Izquierdo-Roca, X. Fontane, L.V. Volkova, E. Arushanov, A. Perez-Rodriguez, Sci. Rep. **6**, 19414 (2016)
60. A. Khare, B. Himmetoglu, M. Cococcioni, E.S. Aydil, J. Appl. Phys. **111**, 123704 (2012)
61. E. Kroumova, M.I. Aroyo, J.M.P. Mato, A. Kirov, C. Capillas, S. Ivantchev, H. Wondratschek, Phase Transitions **76**, 155 (2003)
62. J. Ibanez, R. Oliva, F.J. Manjon, A. Segura, T. Yamaguchi, Y. Nanishi, R. Cusco, L. Artus, Phys. Rev. B **88**, 115202 (2013)
63. B.C. Giessen, C. Borromee-Gautier, J. Sol. St. Chem. **4**, 447 (1972)
64. M.S. Miao, W.R.L. Lambrecht, Phys. Rev. Lett. **94**, 225501 (2005)
65. A. Mujica, A. Rubio, A. Muñoz, R.J. Needs, Rev. Mod. Phys. **75**, 863 (2003)
66. A.M. Hofmeister, Geophys. Res. Lett. **20**, 635 (1993)
67. I.V. Aleksandrov, A.F. Goncharov, A.N. Zisman, S.M. Stishov, JETP **66**, 384 (1987)
68. E. Stavrou, M.R. Manaa, J.M. Zaug, I.-F.W. Kuo, P.F. Pagoria, B. Kalkan, J.C. Crowhurst, M.R. Armstrong, J. Chem. Phys. **143**, 144506 (2015)
69. M.O. Filso, E. Eikeland, J. Zhang, S.R. Madsen, B.B. Iversen, Dalt. Trans. **45**, 3798 (2016)
70. S.N. Vaidya, G.C. Kennedy, J. Chem. Phys. **55**, 987 (1971)
71. M.A. Tuktabiev, S.V. Popova, V.V. Brazhkin, A.G. Lyapin, Y. Katayama, J. Phys. Cond. Matter **21**, 385401 (2009)
72. T. Gurel, C. Sevik, T. Cagin, Phys. Rev. B **84**, 205201 (2011)
73. O. Gomis, D. Santamaria-Perez, R. Vilaplana, R. Luna, J.A. Sans, F.J. Manjon, D. Errandonea, E. Perez-Gonzalez, P. Rodriguez-Hernandez, A. Muñoz, I.M. Tiginyanu, V.V. Ursaki, J. Alloys Compd. **583**, 70 (2013)
74. O. Gomis, R. Vilaplana, F.J. Manjon, D. Santamaria-Perez, D. Errandonea, E. Perez-Gonzalez, J. Lopez-Solano, P. Rodriguez-Hernandez, A. Muñoz, I.M. Tiginyanu, V.V. Ursaki, Mater. Res. Bull. **48**, 2128 (2013)
75. A. Dewaele, M. Torrent, P. Loubeyre, M. Mezouar, Phys. Rev. B **78**, 104102 (2008)
76. I. Erdem, H.H. Karta, T. Cagin, J. Alloys Compd. **587**, 638 (2014)
77. F.D. Stacey, B.J. Brennan, R.D. Irvine, Geophys. Surv. **4**, 189 (1981)
78. A. Bera, K. Pal, D.V.S. Muthu, S. Sen, P. Guptasarma, U.V. Waghmare, A.K. Sood, Phys. Rev. Lett. **110**, 107401 (2013)
79. A. Bera, A. Singh, S.N. Gupta, K. Glazyrin, D.V.S. Muthu, U.V. Waghmare, A.K. Sood, J. Phys. Cond. Matter **33**, 065402 (2021)